applied sciences

MDPI

Article

Finite Element Analysis of Punching Shear of Reinforced Concrete Slab–Column Connections with Shear Reinforcement

Yueqiao Jia * and Jeffrey C. L. Chiang

Faculty of Engineering, Built Environment & Information Technology, SEGi University, Kota Damansara, PJ, Kuala Lumpur 47810, Selangor, Malaysia
* Correspondence: yueqiao1993@gmail.com

Abstract: Shear reinforcement is one of the common measures used to strengthen slab–column connections. It can make the joint's load capacity increase. However, when the connection is subjected to an unbalanced bending moment, the reduction effect of the shear reinforcement on the bending moment is worth investigating. Nonlinear finite element analysis was performed on reinforced concrete slabs with shear reinforcement for various moment-to-shear (M/V) ratios. The effects of the number and diameter of shear reinforcement and different loading methods on the slab were investigated, as along with a correction to the ACI-318 and China Concrete Structure Design code GB50010 formula for the moment transfer coefficient. The 3D finite element modeling was performed using appropriate element types and a constitutive model for concrete. The concrete damage plasticity model parameters were calibrated using the experimental results of a specimen. The amount of shear reinforcement had a certain contribution to the strength of the slab, but the diameter of the shear reinforcement had little effect. The plate's bearing capacity decreased as the M/V increased. The corrected moment transfer coefficient formula demonstrates that M/V is positively correlated with the coefficient and that the calculated values specified in ACI-318 and GB50010 are overly conservative.

Keywords: finite element method; moment transfer; punching shear; slab–column connection; shear reinforcement

Citation: Jia, Y.; Chiang, J.C.L. Finite Element Analysis of Punching Shear of Reinforced Concrete Slab–Column Connections with Shear Reinforcement. *Appl. Sci.* **2022**, *12*, 9584. https://doi.org/10.3390/app12199584

Academic Editor: Laurent Daudeville

Received: 22 August 2022
Accepted: 20 September 2022
Published: 24 September 2022

1. Introduction

The system of reinforced concrete slabs and columns is now widely used worldwide. The benefit of such a system is that the floor is directly supported by columns, there are no beams to block the light, and space is saved. However, the high forces at the slab–column joints lead to high stresses around the columns, making punching shear damage possible [1–4]. Asymmetry of the span or load causes eccentric punching shear in the practical application of the structure. In addition to vertical shear force, the structure is subject to bending moment action, as illustrated in Figures 1 and 2. Punching resistance is reduced by the transfer of the unbalanced bending moment. Moe (1961) [2] first proposed the transfer coefficient of unbalanced bending moment γ_v in his study, believing that γ_v fit well with all of his experimental sample results at 0.33. With subsequent research by Hanson and Hanson (1968) [5], a formula was established in 1970—the ACI-318 [6] design specification—and has been used ever since. The formula shows that its magnitude is only related to the geometry (Equation (1)).

$$\gamma_v = 1 - \frac{1}{1 + \frac{2}{3}\sqrt{\frac{c_1+d}{c_2+d}}} \quad (1)$$

where c_1 and c_2 are the side lengths of the column, and d is the effective thickness of the slab.

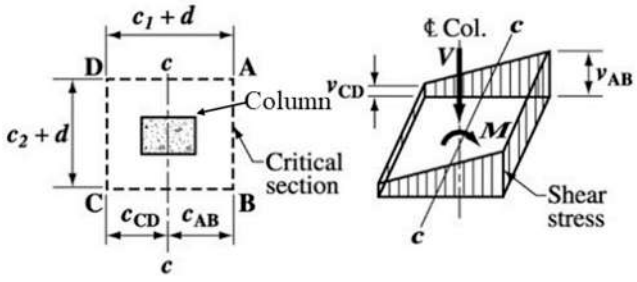

Figure 1. Assumed distribution of shear stress from ACI-318.

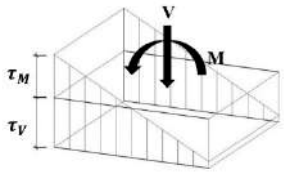

Figure 2. Eccentric shear stress model under vertical load V and unbalanced bending moment M.

Most of the existing studies on slab–column joints used modeling methods. There are many constitutive models for finite element simulation, such as plastic models, nonlinear elastic models, and damage and plastic models [7–9]. H. Park and K. Choi (2006) [10] performed a study on the moment-carrying capacity of slab–column connections using many existing experimental data and nonlinear finite element analysis methods; the numerical simulation results were satisfactory, but whether the moment transfer coefficient specified in ACI-318 is related to other factors has not been discussed in the literature. From Equation (1), it can be seen that the ACI-318 code equation specifies that γ_v is only related to the geometry of the slab–column connection, so the purpose of this study was to explore the relationship between the moment transfer coefficient and other influencing factors, such as shear reinforcement. Since experiments can be expensive and stochastic in terms of financial and material resources, the slab–column connections were modeled using the commercial finite element software ABAQUS [11]. The post-processing cloud image could depict the crack development process, draw deflection curves, and monitor variables that were not measured during the experiment. To describe the tensile and compressive behavior of the concrete, the concrete damage plasticity model was chosen and built into the ABAQUS library. The model parameters were calibrated by comparing the experimental data with the simulation results [12–14]. The nonlinear finite element method was used to investigate the effect of shear reinforcement on the moment transfer coefficient as a supplement to existing building design code formulations, which is the main contribution of this paper.

Two experiments with different loading methods were simulated. Six interior slab–column connections (S1, S2, S3, S4, S7, and S8) equipped with shear reinforcement as described by Ferreira et al. (2019) [15] were analyzed. The variables studied were the number and diameter of the shear studs. In order to better investigate the shear studs, a numerical simulation model was used to increase the number of each variable. The loading method was the force directly applied to the slab. The experiments described by J. Tian and K.B. Xu (1999) [16] were conducted by applying loads to columns, with the variables being the number of studs and their arrangement. The experiments only applied concentric forces, so bending moments were included in the numerical simulations for the study. The variables included in these two experiments are relatively comprehensive in the experiments of shear reinforcement, so they were chosen to simulate and output the experimentally unmeasured data to study the relationship between the moment transfer coefficient and shear reinforcement, which is currently a gap in the study of slab–column connections.

2. Finite Element Simulation

2.1. Test Specimens

The slabs (S1, S2, S3, S4, S7, and S8) were tested as described by Ferreira et al. [15], and the information on the experimental specimens is shown in Table 1. The upper and lower ends of the column were completely fixed, the slab edge was free, and the load was directly applied near the slab edge in these full-scale isolated slab–column joints. Controlling the magnitude of the force applied on each side, as shown in Figure 3c,d, allows for either concentric or eccentric loading. Four jacks, each connected to a loading beam, applied downward force to two shims on each side of the slab. A schematic diagram of eccentric loading can be found in Figure 3d. In the east–west direction, the forces were equal in magnitude. The north and south forces were 0.4 P and 0.1 P, respectively. The total load applied to the plate is denoted by the letter P. Punching shear damage was present in all of the slabs.

Table 1. Characteristics of the Ferreira et al. test slabs.

Specimen	Type of Load [1]	Concrete	Flexural Reinforcement			Shear Studs		
		f_c, MPa	f_y, MPa	E_s, GPa	ρ (%)	Studs [2]	f_{ys}, MPa	E_{ss}, GPa
S1	C	48.3	540	213	1.46	∅10 × 2	535	211
S3	E	50.3			1.46			
S2	C	49.4			1.48	∅10 × 4		
S4	E	49.2			1.48			
S7	C	48.9			1.48	∅12.5 × 4	518	204
S8	E	48.4			1.47			

[1] C: concentric loading, E: eccentric loading. [2] The number after ∅ indicates the diameter of the stud (mm), while the number after × indicates the number of studs in a row.

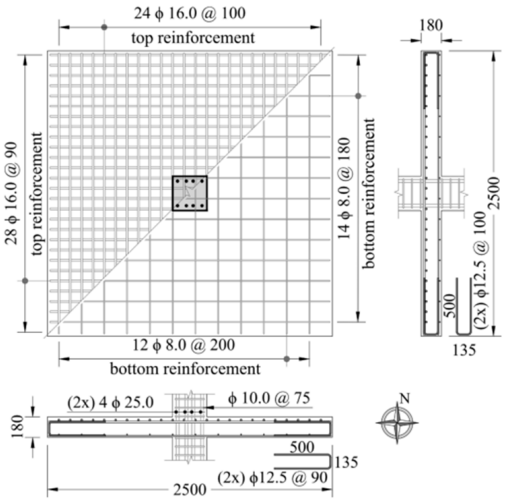

(**a**)

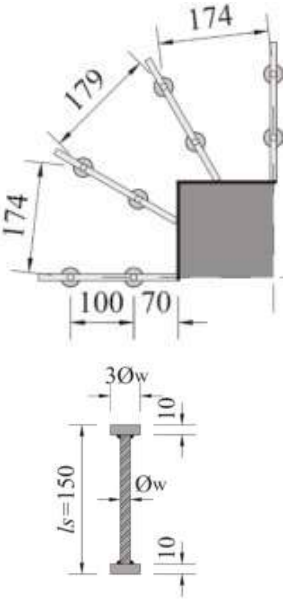

(**b**)

Figure 3. *Cont.*

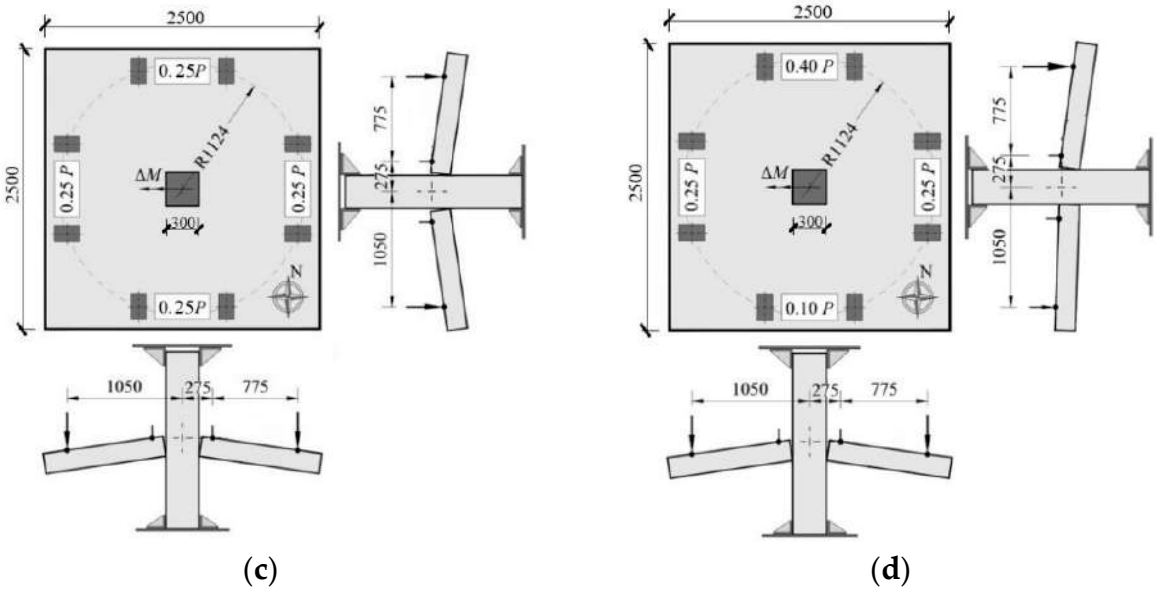

Figure 3. Schematic illustrations of the specimens of Ferreira et al.: (**a**) detailing of the flexural reinforcement; (**b**) shear reinforcement of the slabs (the gray square is the quarter column); (**c**) concentric loading pattern for slabs; (**d**) eccentric loading pattern for slabs [15].

The six square plates used in this paper had a side length of 2500 mm and a thickness of 180 mm, with an effective thickness of approximately 145 mm. The square column had a side length of 300 mm. The reinforcement layout is shown in Figure 3a. With a steel sheet, the shear studs were welded together in pairs. The stud assemblies were radially distributed around the column, as shown in Figure 3b.

The concentric load was applied directly to slabs P1, P2, P3, P4, and P5 at the head of the column tested by J. Tian and K.B. Xu (1999) [16] (Figure 4a). The side length of the square slab was 2000 mm and the thickness of the plate was 160 mm. However, for P4, the plate thickness was 180 mm. The column size was 250 × 250 mm, located in the center of the plate and extending 400 mm from the top and bottom of the slab. The bending reinforcement of the slab was 16 mm diameter reinforcement with 180 mm spacing arrangement, and the yield strength was 370 MPa. The shear studs of P1 and P3 were arranged as shown in Figure 4b, while the shear studs of P2, P4, and P5 were arranged as shown in Figure 4c. The diameter of the shear studs was 10 mm. Other details of the specimens are shown in Table 2.

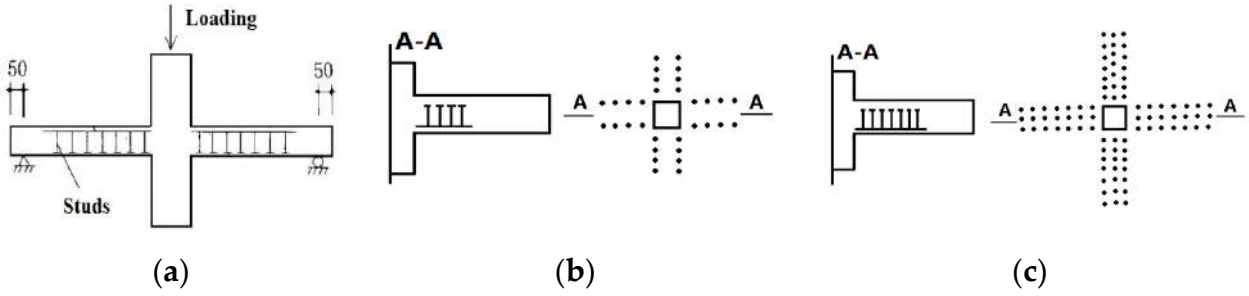

Figure 4. Schematic drawings of the specimens of J. Tian and K.B. Xu: (**a**) loading diagram; (**b**) shear stud arrangement 1; (**c**) shear stud arrangement 2.

Table 2. Characteristics of the J. Tian and K.B. Xu test slabs.

Specimen	f_c, MPa	Distance of the First Row of Studs from the Column Surface, mm	Studs' Spacing, mm	Number of Studs on Each Steel Plate
P1	24	68	101	4
P2	24	68	75	7
P3	25	47	68	9
P4	25.1	54	78	9
P5	25.3	47	68	7

2.2. Methodology

The steps shown in Figure 5 are required for numerical simulations using the finite element software ABAQUS [11]. In numerical simulations, the model can abort the calculation in a variety of ways. The reasons for this could all be related to the ways in which certain steps are set up in the model, causing it to fail to converge (see the area indicated by the "No" arrow). The following are the steps of the experiment simulated in this paper:

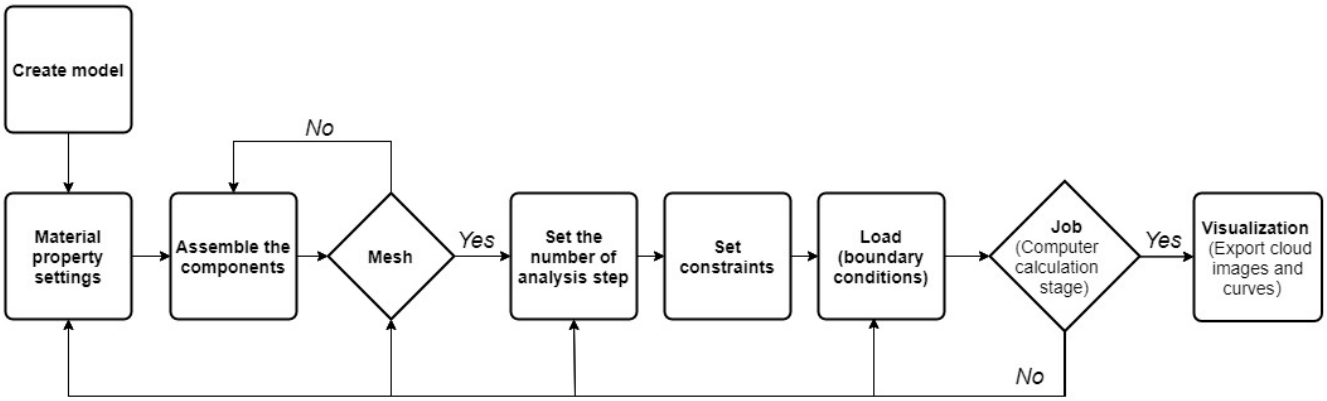

Figure 5. Simulation flowchart.

Step 1. Create model: Modeling based on the geometry given in the experiment.

Step 2. Material property settings: The properties of the materials are input as described in the experiment. The damage plasticity model is used to describe the concrete, and its input parameters must be calibrated, as explained in Section 2.4.

Step 3. Assemble the components: The assembly of the components requires attention as to the direction of the coordinates.

Step 4. Mesh: The model is divided into meshes that need to be cut into regular shapes in advance. The concrete and reinforcement elements need to be typed. One element type is the completely integral element, and when the element has a regular shape, the number of Gaussian integral points used is sufficient to precisely integrate the polynomial in the element stiffness matrix. The disadvantage is that under bending load there will be shear self-locking, resulting in the element being too rigid, even with the division of a very fine grid, so the calculation accuracy is still very poor. The other type is the reduced integral element, which uses one less integral point in each direction than the normal full integral element, has only one integral point in the center of the element, and is too soft due to the hourglass value problem (Figure 6). When a linear integral element is used to simulate a structure subjected to bending load, at least four elements should be divided along the thickness direction. According to the grid sensitivity test conducted by Genikomsou (2015) [17], the smaller the grid size, the earlier the component is destroyed—that is, the smaller the deflection or rotation. After experience verification, it is sufficient to ensure 4 grids in the thickness direction. Therefore, the mesh sizes of the two experimental models simulated in this paper were 45 and 40, respectively, as shown in Figure 7. The 8-noded

hexahedral (brick) reduced integral elements, C3D8R, were used for simulating concrete, where C represents the solid element, 3D means three-dimensional, 8 is the number of nodes in this unit, and R represents this unit as a reduced integral unit. The 2-node linear truss element, T3D2, was used to model the reinforcement. The choice of the element type of shear studs needed to be trialed, as shown in Figure 8, using solid and truss elements to simulate the shear studs. The load–displacement curves (Figure 9) show that the solid elements failed prematurely, did not contribute to the strength of the slab, and were less ductile. The results of the truss elements simulating the shear studs were similar to the experimental values. Therefore, truss elements were used for the simulation of shear reinforcement in this study.

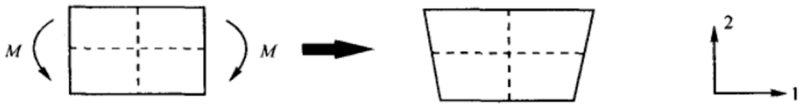

Figure 6. Linear reduced integration element subjected to bending moment.

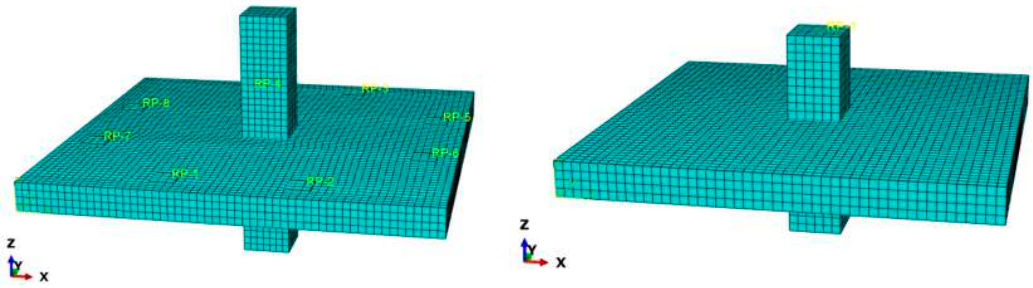

(**a**) (**b**)

Figure 7. Mesh division: (**a**) Model of Ferreira et al. (**b**) Model of J. Tian and K.B. Xu.

(**a**) (**b**)

Figure 8. Different element types for shear studs: (**a**) solid elements; (**b**) truss elements.

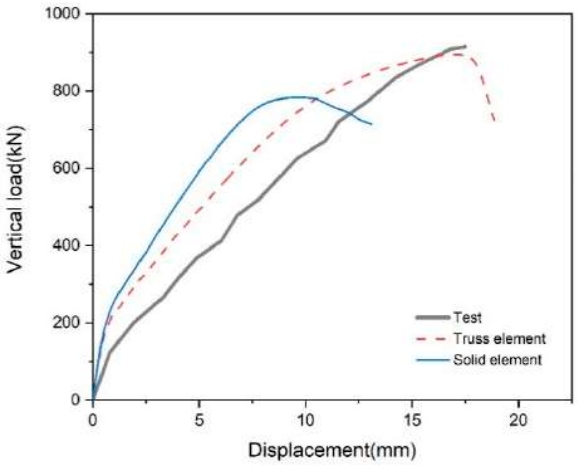

Figure 9. Load–deflection response of slab S1 with different element types.

Step 5. Set step: Sets the initial incremental step size and the maximum number of incremental steps. The purpose is to prevent the model from failing to converge in the calculations. The maximum number of incremental steps can be set to 1000 or 10,000, and the initial incremental size can be set to 0.01 or 0.001 [11].

Step 6. Set the constraint: The bond between the concrete and the reinforcement is modeled using the embedded method. The shear studs simulated with truss units are also embedded with the concrete constraints. The TIE constraint is used between the column and the plate—that is, there is no relative sliding between the two at the joint. TIE is also used between the shims and the slab. For determining the shear stud element type, the mutual constraints of the different parts of the shear stud simulated with solid units and their constraints with concrete are TIE. Coupling constraints are used between the loading point and the shim—that is, the load on the point is uniformly loaded on the shim surface.

Step 7. Load: The loading method is displacement loading. Compared with direct loading of concentrated force, the model converges more easily. The boundary conditions are also set in this step. The boundary conditions are set to limit the displacement of the model, including the translational and rotational degrees of freedom, and to limit the degrees of freedom by making the restricted direction equal to 0. For the experiment described by Ferreira et al., the column is completely fixed on the top and the bottom, so the boundary condition is set to U1 = U2 = U3 = UR1 = UR2 = UR3 = 0 (U1 = 0 means that the displacement in the x-direction is limited; UR1 means that the rotation around the *x*-axis is limited; 2 and 3 represent the y- and z-directions). The vertical load is applied to the 8 shims near the edge of the plate, as in the experimental setup, as shown in Figure 10a. For the experiment of J. Tian and K.B. Xu [16], the plate is simply supported on all four sides and the column is free at both ends. Therefore, the degrees of freedom of the four sides of the plate are limited to U1 = U2 = U3 = 0. Since the experiment of J. Tian and K.B. Xu [16] only applies vertical concentrated force to the column, it is extended in this paper using numerical simulation. Transverse forces of equal magnitude and opposite directions are applied at both ends of the column to simulate the bending moment. The magnitudes of the vertical and transverse forces are controlled to obtain the load-carrying cases of the slab for different values of M/V, as shown in Figure 10b.

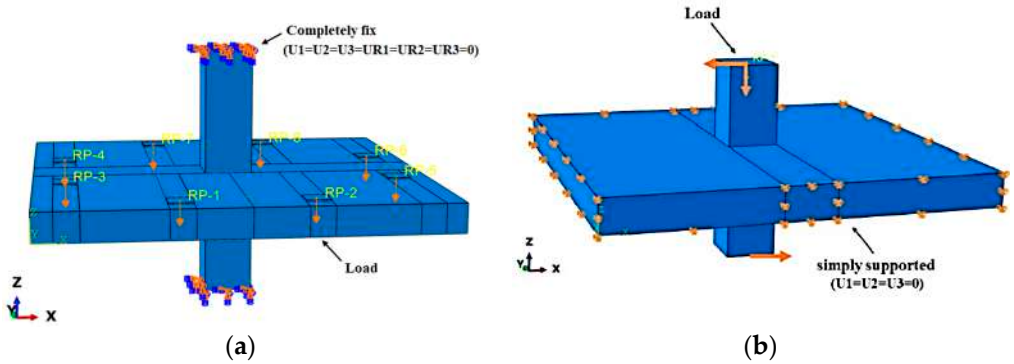

Figure 10. Load and boundary conditions in ABAQUS: (**a**) Ferreira et al.'s specimens; (**b**) J. Tian and K.B. Xu's specimens.

Step 8. Submit a job—that is, submit the calculation to the computer.

Step 9. Visualization: After processing, the crack pattern and function curve can be displayed. In the concrete damage plasticity model, it is specified that the concrete cracks when the plastic strain is greater than 0, so PE (plastic strain ε) can be used to view the concrete's cracks.

2.3. Concrete Damage Plasticity Model

The concrete damage plasticity model (CDP) is a model built into ABAQUS to describe the nonlinear behavior of concrete. It was first proposed by Lubliner et al. [18] as the Barcelona model, and it is based on using fracture energy to represent all damage states. The

concrete damage plasticity model introduces damage factors into the concrete model and discounts the elastic stiffness matrix of concrete to simulate the decrease in the unloading stiffness of concrete with increasing damage. This model requires the input of stresses and inelastic strains ε_c^{in} as well as the damage factor in ABAQUS. These feature data associated with the uniaxial tensile and compressive stress–strain curves for concrete, as shown in Figure 11. The initial stage is elastic, no damage occurs, and the stiffness is E_0. As shown in Figure 11a, when the stress exceeds the elastic limit stress σ_{co}, it enters the strengthening stage. When the stress exceeds the limiting stress σ_{cu}, it enters the softening stage, where the concrete produces compression damage, and the unloading stiffness becomes $(1 - d_c)E_0$. As shown in Figure 11a, $\varepsilon_c^{in} = \varepsilon_c - \frac{\sigma_c}{E_0}$ and $\varepsilon_c^{pl} = \varepsilon_c^{in} - \frac{d_c}{1-d_c}\frac{\sigma_c}{E_0}$; therefore, $\varepsilon_c^{el} = \varepsilon_c - \varepsilon_c^{pl}$. From the above three formulae, $d_c = 1 - \frac{\sigma_c}{\varepsilon_c^{el}}/E_0$ can be obtained. Similarly, the tensile damage factor d_t can also be derived via this method, as shown in Figure 11b. $d_t = 1 - \frac{\sigma_t}{\varepsilon_t^{el}}/E_0$.

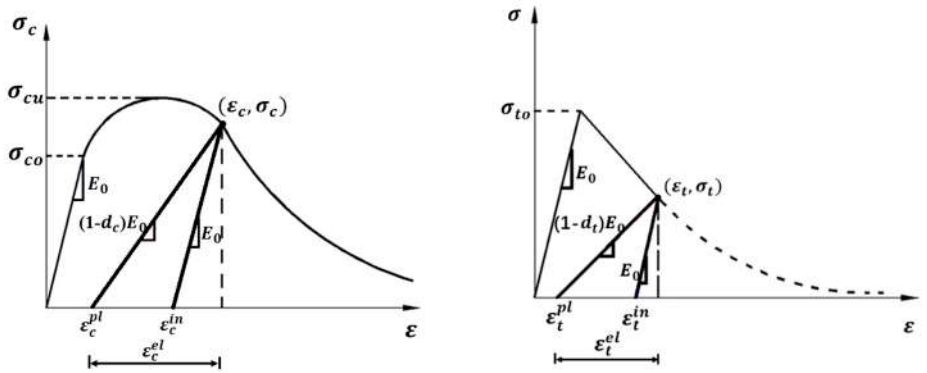

(**a**) (**b**)

Figure 11. Uniaxial stress–strain curves for concrete: (**a**) uniaxial compressive stress–strain curve of concrete; (**b**) uniaxial tensile stress–strain curve of concrete.

The calculation of stress and strain depends on the constitutive model of concrete. In this paper, the constitutive equation for concrete provided in the Chinese Code for Concrete Structure Design GB50010-2010 [19] is used for the calculation. The detailed equations are listed in Appendix A. The calculated input CDP parameters, concrete stress–strain curve and damage factors are shown in Appendix B.

2.4. Calibration of CDP Parameters

When the concrete damage plasticity model is used to simulate the cracking behavior of concrete, two parameters—the dilation angle and the viscosity parameter—need to be calibrated to ensure the accuracy of the simulation. The dilation angle ψ in the CDP model of this paper is set to simulate the volume expansion of concrete as a brittle material due to inelastic strain when subjected to tension. A larger dilation angle indicates more brittle concrete. Wu et al. [20] defined the dilation angle for reinforced concrete, and its value was specified from 31° to 42°. The recommended values in the ABAQUS user manual [11] are 30–45°. The viscosity parameter μ is a time-dependent parameter that controls the convergence of the model and the accuracy of the calculation. When μ is equal to 0, the material is purely plastic; when μ is equal to 1, the material is purely elastic. The smaller the value, the more precise the accuracy, and the more the speed of the calculation decreases. The recommended values in ABAQUS [11] range from 0.00001 to 0.005.

For the experiments of Ferreira et al. (2019), the parameters are calibrated based on the S1 slab. Figure 12a shows the results from simulations with different dilation angles. All of the dilation angle results in Figure 12a were obtained at $\mu = 0.0001$, where μ is at a relatively accurate level, and the curves for $\psi = 30^{\circ}$ and $\psi = 35^{\circ}$ both have peaks and fall rapidly, demonstrating that damage to the slab has occurred and does not fit with the experimental curve. The comparison shows that $\psi = 40^{\circ}$ can simulate the experimental

results relatively accurately. Figure 12b shows the simulation results for different viscosity parameters. The smaller the viscosity parameter, the more accurate the results. Figure 13 shows a good correlation between the post-processed cloud image and the photographs of the cracks. The results of Figure 13 are simulated for $\psi = 40^{\circ}$, $\mu = 0.0001$. The numerical simulation can accurately simulate tangential cracks on the face of the slab, and the ring cracks are formed outside the shear reinforcement region (the red bar is the location of the shear studs), which is consistent with the description of the experimental results. Therefore, $\psi = 40^{\circ}$, $\mu = 0.0001$ was finally determined and applied to all of the model simulations of Ferreira et al. For J. Tian and K.B. Xu's experiment, relatively accurate simulation results were obtained using $\psi = 40^{\circ}$, $\mu = 0.005$. The results of the comparison of the experimental results from P1 to P5 with the simulated values can be seen in Figure 20.

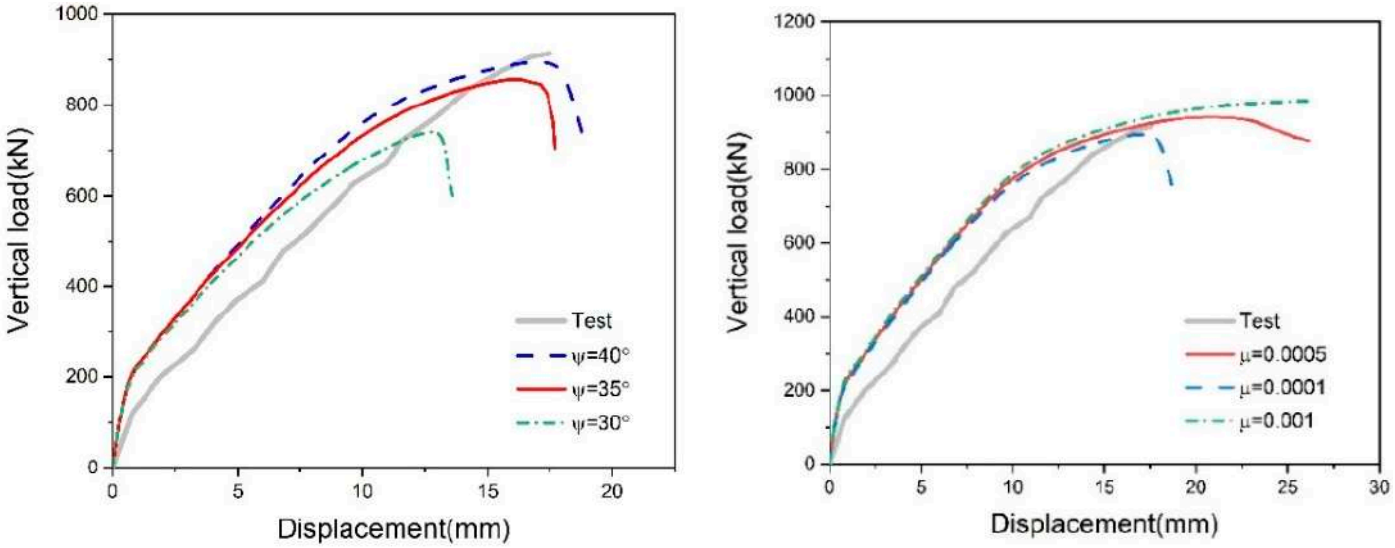

(**a**) (**b**)

Figure 12. Parameter calibration of the S1 slab: (**a**) dilation angle; (**b**) viscosity parameters.

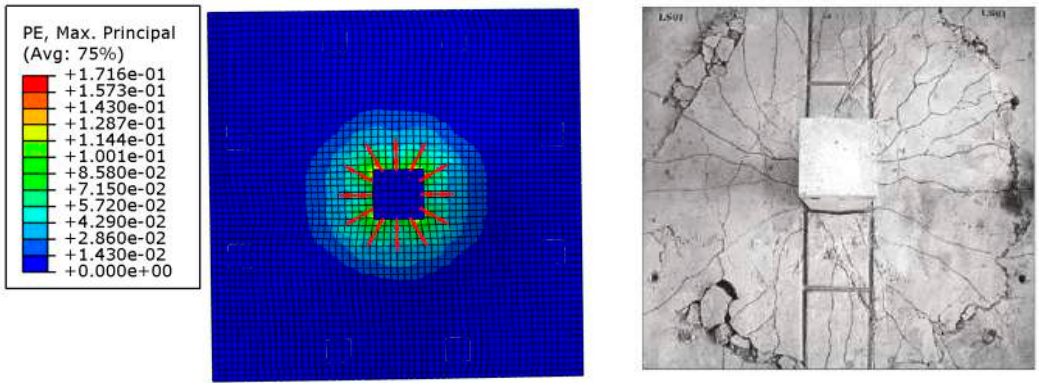

(**a**) (**b**)

Figure 13. Tension-side view of the specimen S1 experiment and FEA crack patterns: (**a**) simulation result; (**b**) test result [15].

3. Finite Element Model Validation

3.1. Crack Pattern

Figures 14–18 show experimental crack photographs compared to the simulation results for S2, S3, S4, S7, and S8. By highlighting the shear reinforcement, it is easy to see whether the cracks are within the shear zone. The S2, S3, S4, and S8 slabs all have cracks inside the shear zone, whereas the S7 slab has cracks outside the shear zone, according

to the experimental results. When comparing the photos to the experimental results, the cracks are visibly in similar locations. The experimental results are similar to the cracks in the simulated plates with concentric force (i.e., S2 and S7). A visible ring of closed cracks is formed around the column, which is typical of punching shear damage. The crack simulation results for the eccentric force plate S3 are consistent with the experimental results, with an asymmetric shape of the cracks due to eccentric loading. However, the crack patterns of S4 and S8, which are also subjected to eccentric forces, can show circular cracks near the columns, but the overall crack similarity is different. This may be due to the increase in the number of shear studs, which leads to sliding in the outer two rings of the shear studs in the plate under actual conditions. While the ABAQUS simulation assumes that the reinforcement and concrete are embedded constraints, this is an ideal state. Because there is no relative slip, the cracking is symmetrical, and the cracks on the eccentric force side are more developed. The change in color in the post-processed image PE of ABAQUS indicates the degree of damage. The location of the crushed concrete in the experimental photo shows a dark color at the same location in the FEA image, indicating the validity of the simulation. Therefore, from the comparison of the crack patterns, the numerical simulation can be infinitely close to the actual results, although it cannot completely restore the experimental results. The error is within the acceptable range, and the results are still reliable.

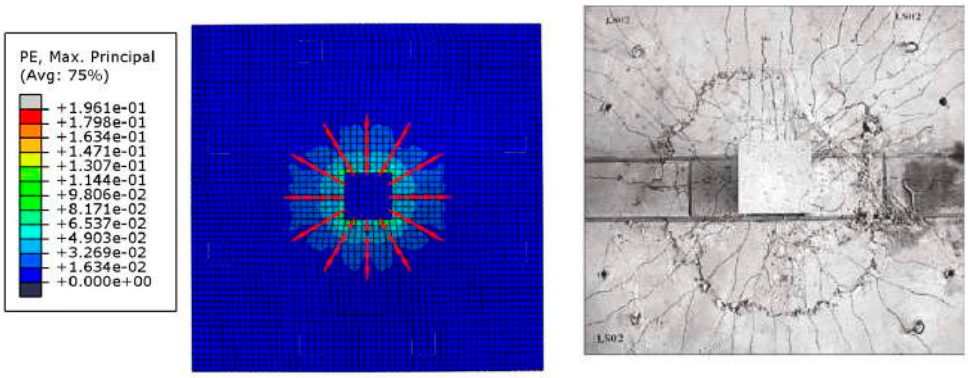

(**a**) (**b**)

Figure 14. Tension-side view of the specimen S2 experiment and FEA crack patterns: (**a**) simulation result; (**b**) test result [15].

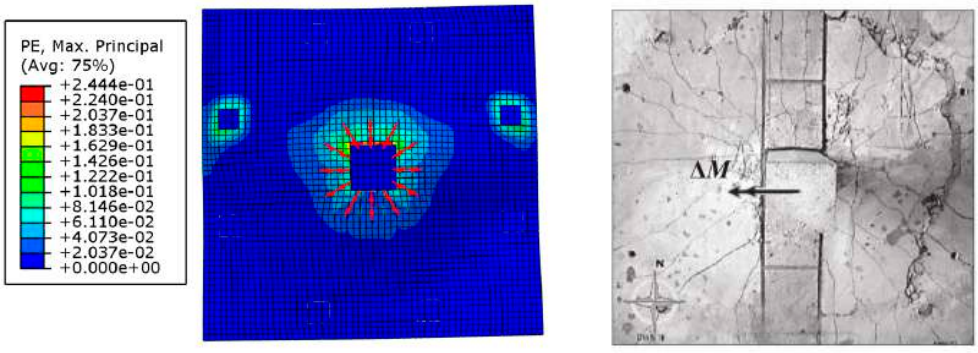

(**a**) (**b**)

Figure 15. Tension-side view of the specimen S3 experiment and FEA crack patterns: (**a**) simulation result; (**b**) test result [15].

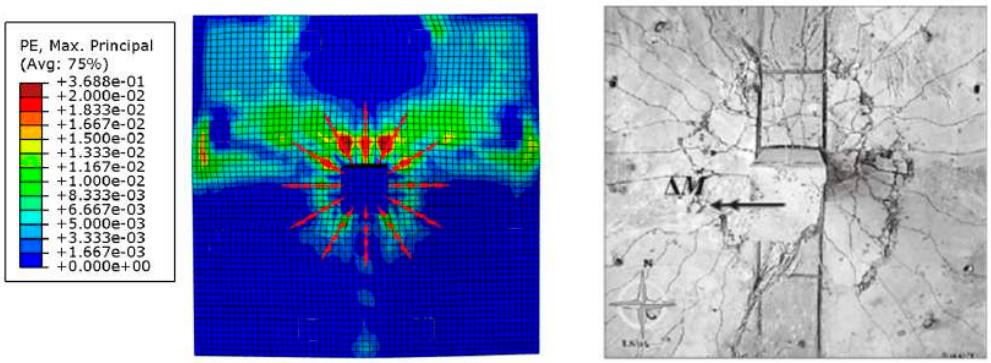

Figure 16. Tension-side view of the specimen S4 experiment and FEA crack patterns: (**a**) simulation result; (**b**) test result [15].

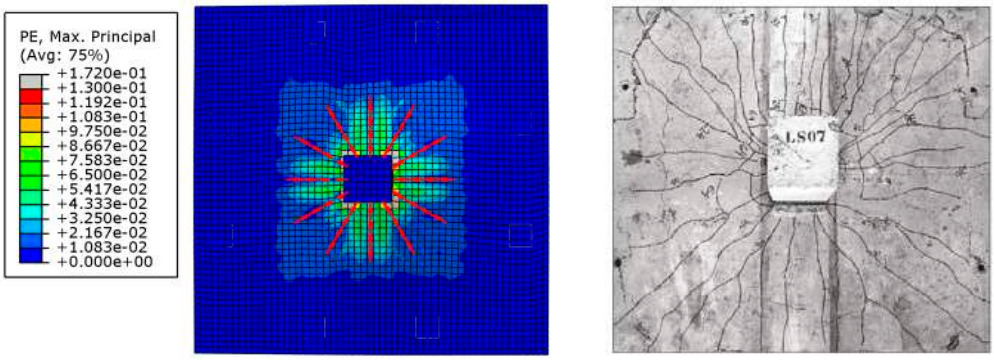

Figure 17. Tension-side view of the specimen S7 experiment and FEA crack patterns: (**a**) simulation result; (**b**) test result [15].

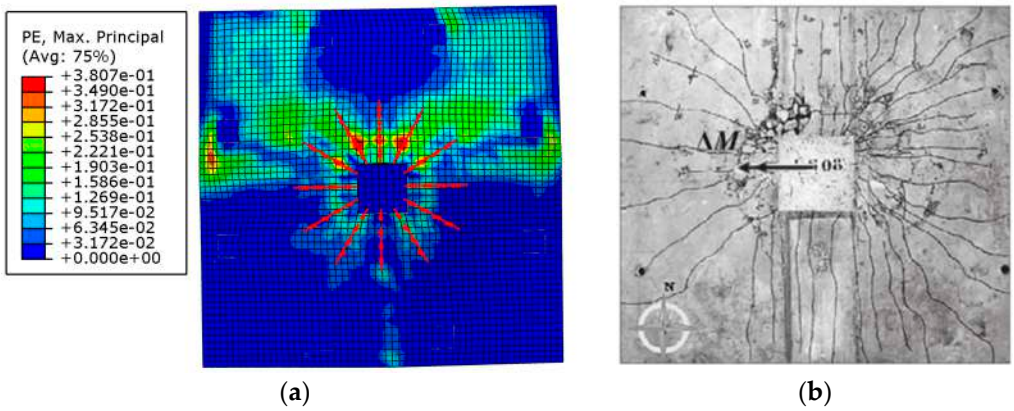

Figure 18. Tension-side view of the specimen S8 experiment and FEA crack patterns: (**a**) simulation result; (**b**) test result [15].

Since the experimental results of J. Tian and K.B. Xu (1999) [16] do not show the crack photos of the slabs, there is no crack comparison here.

3.2. Load–Deflection Response

According to Ferreira et al.'s experimental results presented in the literature, the V_u values for S2, S3, S4, S7, and S8 are 1127 kN, 699 kN, 722 kN, 1197 kN, and 734 kN, respectively. This includes 37.5 kN of the equipment's self-weight. As the numerical simulations use ideal state loading, the simulated results should be compared with the load

values without the 37.5 kN included. The simulated values for these plates are 1159 kN, 650 kN, 687 kN, 1142 kN, and 717 kN, respectively, with 1.06, 0.98, 1.00, 0.98, and 1.03 as the ratios to the experimental values, respectively. There is also little difference in the displacements. Therefore, the simulations have a high level of accuracy, confirming the accuracy of the parameters calibrated in the previous section. Figure 19 illustrates the comparison curve between the experimental and finite element model (FEM) results. Simulation of shear studs with truss units seems to improve the ductility of the plates. Figure 19a,d show plates S2 and S7 subjected to concentrated forces, respectively, and the initial stiffness of the curves for the simulated results is slightly greater than the experimental results. There could be many reasons for this, possibly due to the non-uniformity of the material during the casting of the actual experimental samples, the presence of initial cracks, or because the numerical simulations were performed under ideal conditions.

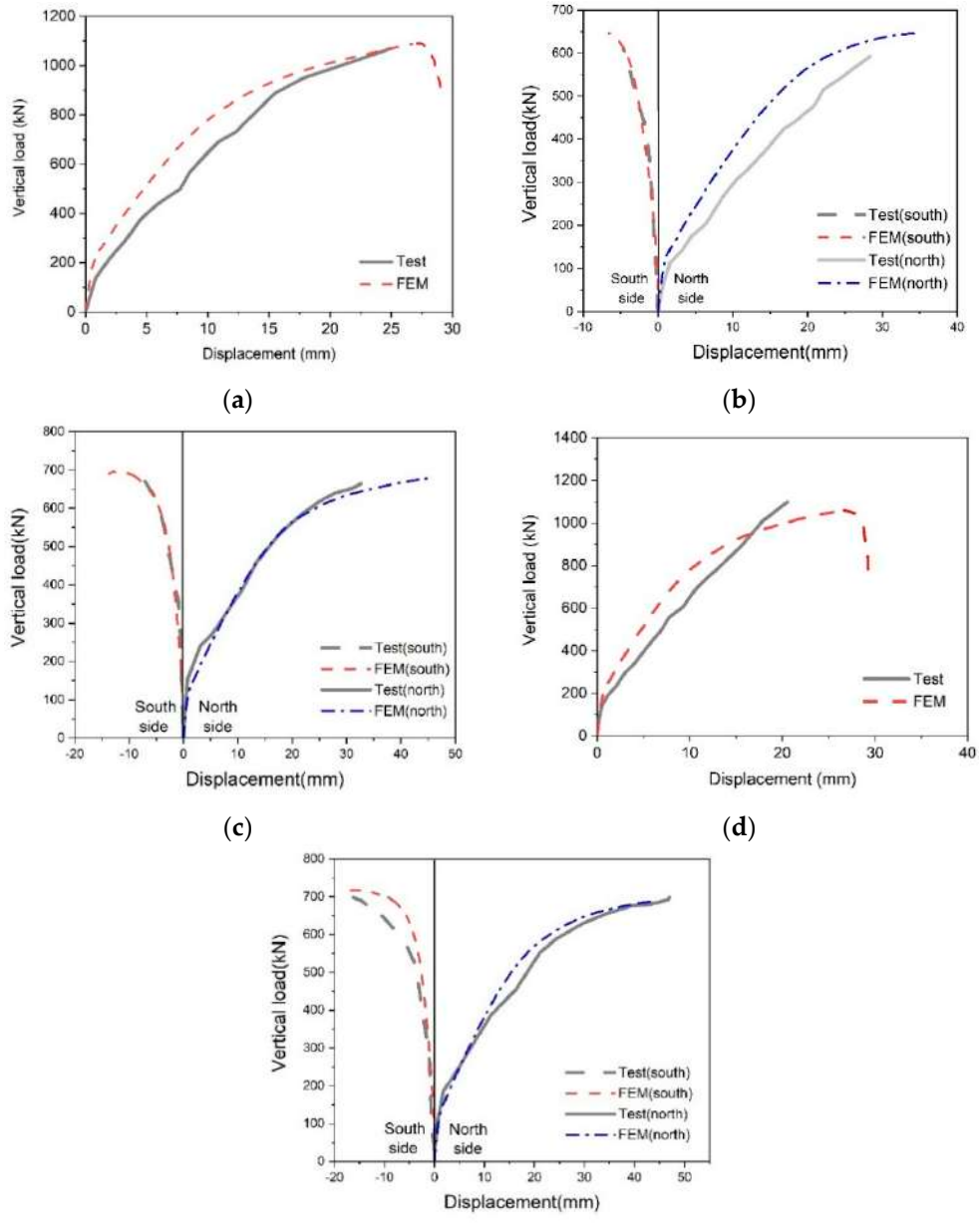

Figure 19. Load−displacement response Ferreira et al.'s experimental results [15] versus FEM: (**a**) S2; (**b**) S3; (**c**) S4; (**d**) S7; (**e**) S8.

For the experiments of J. Tian and K.B. Xu (1999) [16], it can be seen from Figure 20 that the curve shapes of the experimental and simulated results are very similar, and the differences in the ultimate bearing capacity are small. The displacement response is essentially the same, except for P5 (within 10% error). Because of the large amount of shear studs in the P5 arrangement, the experimental results show that the plate is damaged outside the reinforced zone, so the change in deflection is not as pronounced as it is in P1–P4 when the damage is imminent. The numerical simulations were carried out under ideal conditions, and the stiffness and ductility were slightly greater than the experimental results, but were also within acceptable limits. The reliability of the simulation was verified. Therefore, the study of the bending moment can be added to this model. A transverse force of equal magnitude and the opposite direction was applied to both ends of the column to simulate the effect of the bending moment.

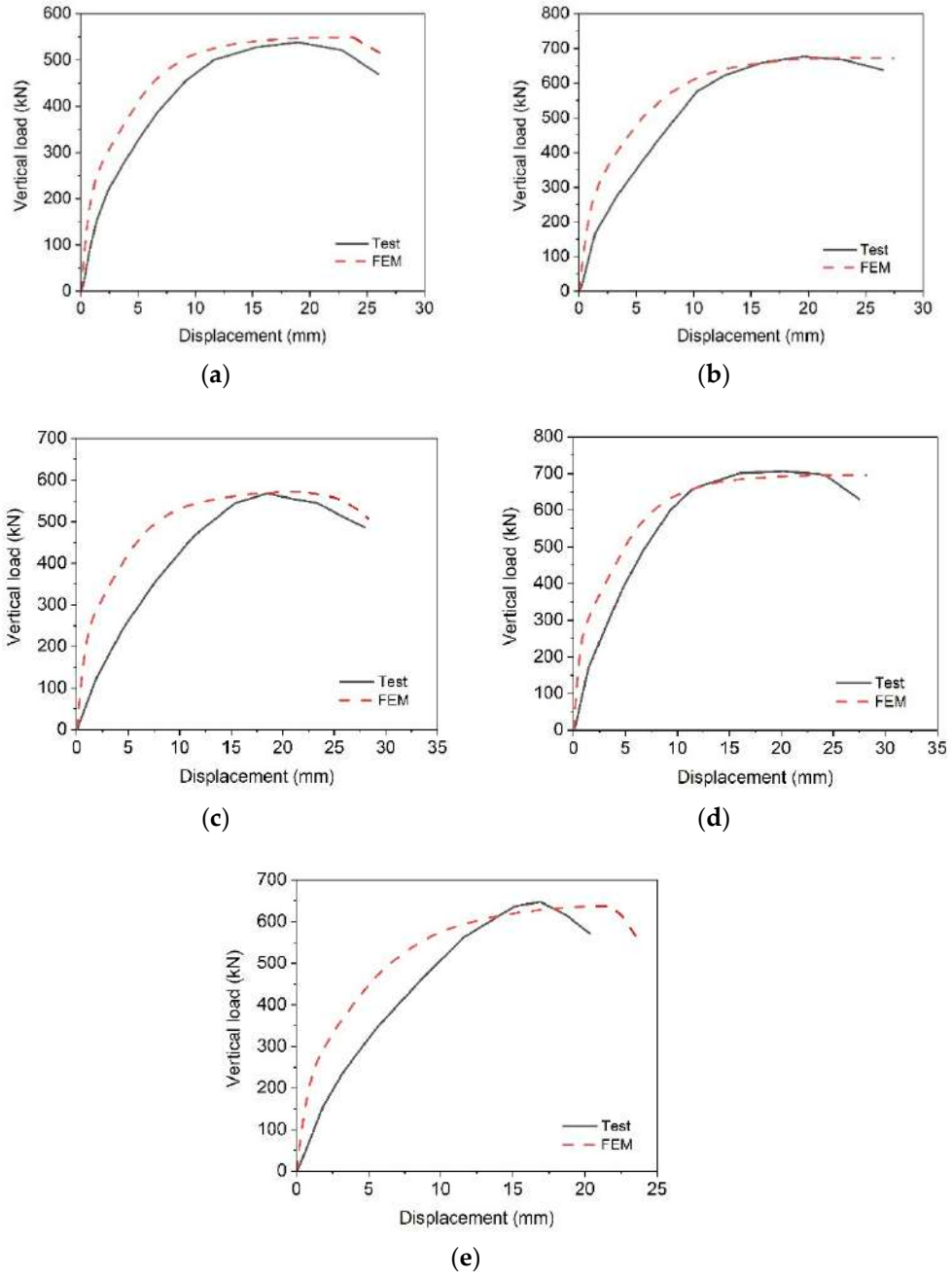

Figure 20. Load–displacement response of J. Tian and K.B. Xu's experimental results versus FEM: (**a**) P1; (**b**) P2; (**c**) P3; (**d**) P4; (**e**) P5.

4. Finite Element Analysis Results and Discussion

4.1. Average Shear Stress in the Critical Section

Most current building codes consider that damage occurs when the shear force in the critical section of the slab exceeds the load-carrying capacity of the slab. Except for Eurocode 2 [21], most design standards take the location of the critical section to be at a distance of d/2 from the column surface. When damage occurs outside the reinforcement zone, b_{out} is the perimeter from the position of the outermost shear reinforcement d/2 (Figure 21). However, the experimental specimens in this paper take only the critical section shear stress on the eccentric force side into account.

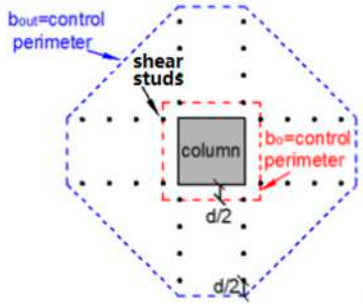

Figure 21. Control perimeter according to ACI-318.

Only the slabs with M/V = 0 (i.e., S1, S2, and S7) and M/V = 0.27 (i.e., S3, S4, and S8) were tested in the experiments of Ferreira et al. The numerical simulation in this paper was carried out by adjusting the forces applied to the four sides of the plate to achieve different moment-to-shear ratios (M/V = 0.36, 0.45, and 0.54). The average shear stress only showed a significant decrease when M/V > 0.36, as shown in Figure 22a. The plates with four shear studs had a higher average shear stress than the plates with two shear studs, implying that increasing the number of shear studs does improve the plate's performance. For a more complete comparison, a set of plates with two 12.5 mm diameter shear studs were added to the test using the finite element software. This shows that the green triangles are slightly higher than the gray squares (two-stud group) and the blue triangles are slightly higher than the red circles (four-stud group). S7 has a lower average shear stress than S2 because it breaks outside the shear reinforcement zone. This suggests that the diameter of the shear studs has only a minor impact on the plate's efficiency. However, the trend of the M/V versus average shear stress curves is similar for the four groups. The average shear stress is essentially constant when M/V is less than 0.36, and it decreases as M/V increases. In this experiment, the maximum M/V simulated was 0.54, with V representing the slab–column connection's self-weight. The specific values are summarized in Table 3. The naming rule for the newly added model is the number of studs—diameter of studs—ratio of M/V. The stresses in the critical section were not measured in this experiment, so the numerical simulation is a complement to the experiment in this respect.

For the simulations of different M/V cases for the experimental samples of J. Tian and K.B. Xu, the average shear stresses on the critical section of the eccentric side plate do not differ much (Figure 22b). The five groups have similar trends. As M/V increases from 0 to 0.5, the average shear stress increases sharply. After that, as M/V increases, the average shear stress tends to level off and has a slight decreasing trend. It can be seen that the arrangement and number of shear studs have no significant effect on the shear stress. However, for Ferreira et al.'s experiment, the effect of increasing the number of studs on the plate is obvious. The reason for this may be because the number of studs set in J. Tian and K.B. Xu's experiment is 4, 7, and 9, where the minimum number already meets the load-bearing requirement. When the joints are subjected to bending moments, too many studs may not contribute much to the effect. The simulated data are shown in Table 3; for experimental samples P1–P5, three different M/V cases were added to the model for each plate, with the naming rule of experimental sample name–studs' diameter–ratio of M/V.

Table 3. Average shear stress and moment transfer coefficient for different values of M/V.

Experience	Specimen	Shear Studs, Number/Diameter	M/V	M, kN·m	V, kN	Average Shear Stress, MPa	γ_{vs}
Ferreira et al. [15]	S1	2 studs/10 mm	0	0	977	2.86	0
	S3		0.27	224	723	2.80	0.095
	2-10-036		0.36	297	824	2.89	0.129
	2-10-045		0.45	337	748	2.72	0.148
	2-10-054		0.54	378	700	2.64	0.161
	S2	4 studs/10 mm	0	0	1159	3.26	0
	S4		0.27	265	687	3.31	0.096
	4-10-036		0.36	339	942	3.29	0.127
	4-10-045		0.45	345	766	2.85	0.155
	4-10-054		0.54	383	709	2.75	0.169
	6-10-0	6 studs/10 mm	0	0	1160	3.23	0
	6-10-027		0.27	270	999	3.32	0.099
	6-10-036		0.36	346	960	3.36	0.128
	6-10-045		0.45	347	770	2.96	0.161
	6-10-054		0.54	389	721	2.82	0.171
	2-12.5-0	2 studs/12.5 mm	0	0	948	2.87	0
	2-12.5-027		0.27	239	884	2.96	0.092
	2-12.5-036		0.36	306	849	2.97	0.128
	2-12.5-045		0.45	344	764	2.77	0.147
	2-12.5-054		0.54	380	704	2.70	0.166
	S7	4 studs/12.5 mm	0	0	1142	3.14	0
	S8		0.27	265	981	3.42	0.113
	4-12.5-036		0.36	341	947	3.39	0.137
	4-12.5-045		0.45	349	777	2.90	0.157
	4-12.5-054		0.54	392	726	2.81	0.168
	6-12.5-0	6 studs/12.5 mm	0	0	1185	3.28	0
	6-12.5-027		0.27	276	1024	3.52	0.115
	6-12.5-036		0.36	359	997	3.52	0.141
	6-12.5-045		0.45	355	788	3.00	0.163
	6-12.5-054		0.54	399	738	2.88	0.171
	2-8-0	2 studs/8 mm	0	0	901	2.67	0
	2-8-027		0.27	211	783	2.62	0.082
	2-8-036		0.36	274	761	2.65	0.116
	2-8-045		0.45	304	675	2.55	0.140
	2-8-054		0.54	341	631	2.51	0.156
	4-8-0	4 studs/8 mm	0	0	1047	3.04	0
	4-8-027		0.27	260	962	3.15	0.092
	4-8-036		0.36	332	923	3.12	0.125
	4-8-045		0.45	339	754	2.71	0.144
	4-8-054		0.54	381	706	2.62	0.167

Table 3. *Cont.*

Experience	Specimen	Shear Studs, Number/Diameter	M/V	M, kN·m	V, kN	Average Shear Stress, MPa	γ_{vs}
Ferreira et al. [15]	6-8-0	6 studs/8 mm	0	0	1108	3.08	0
	6-8-027		0.27	261	966	3.17	0.093
	6-8-036		0.36	334	926.5	3.15	0.127
	6-8-045		0.45	339	754	2.68	0.161
	6-8-054		0.54	381	705	2.60	0.165
	2-15-0	2 studs/15 mm	0	0	991	2.91	0
	2-15-027		0.27	242	897	3.02	0.095
	2-15-036		0.36	313	869	3.01	0.134
	2-15-045		0.45	348	773	2.82	0.149
	2-15-054		0.54	387	717	2.73	0.174
	4-15-0	4 studs/15 mm	0	0	1158	3.25	0
	4-15-027		0.27	276	1023	3.54	0.119
	4-15-036		0.36	355	985	3.52	0.136
	4-15-045		0.45	355	789	2.90	0.151
	4-15-054		0.54	396	733	2.79	0.174
	6-15-0	6 studs/15 mm	0	0	1203	3.39	0
	6-15-027		0.27	306	1132	3.68	0.128
	6-15-036		0.36	387	1076	3.73	0.137
	6-15-045		0.45	383	850	3.05	0.164
	6-15-054		0.54	423	784	2.95	0.181
J. Tian and K.B. Xu [16]	P1	4 studs/s = 101 mm	0	0	541	2.08	0
	P1-10-050		0.50	196	399	2.81	0.125
	P1-10-068		0.68	199	296	2.71	0.177
	P1-10-165		1.65	229	139	2.63	0.259
	P2	7 studs/s = 75 mm	0	0	672	2.42	0
	P2-10-051		0.51	230	450	2.96	0.094
	P2-10-071		0.71	231	325	2.90	0.159
	P2-10-161		1.61	238	148	2.69	0.228
	P3	9 studs/s = 68 mm	0	0	570	2.15	0
	P3-10-049		0.49	198	407	2.91	0.132
	P3-10-068		0.68	206	305	2.80	0.177
	P3-10-146		1.46	209	144	2.61	0.252
	P4	9 studs/s = 78 mm	0	0	700	2.53	0
	P4-10-040		0.40	217	536	2.92	0.095
	P4-10-053		0.53	212	400	2.97	0.162
	P4-10-129		1.29	234	182	2.76	0.275
	P5	7 studs/s = 68 mm	0	0	640	2.20	0
	P5-10-048		0.48	212	445	2.88	0.095
	P5-10-067		0.67	223	331	2.79	0.147
	P5-10-169		1.69	254	150	2.63	0.238

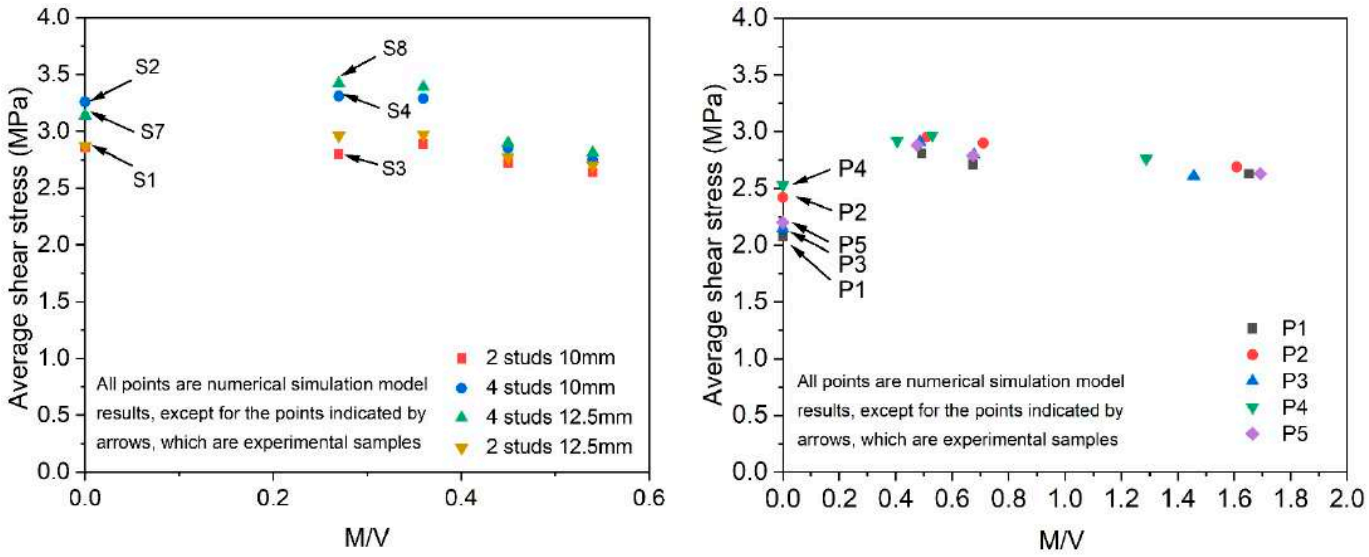

(**a**) (**b**)

Figure 22. Average shear stress versus M/V: (**a**) Ferreira et al.'s slabs (**b**) J. Tian and K.B. Xu's slabs.

4.2. Coefficient of the Bending Moment Transferred by the Eccentric Shear Force

As shown in Figures 1 and 2, the shear stress on the critical section is composed of the shear stress generated by the vertical load and the additional shear stress generated by the action of the unbalanced bending moment, as defined by ACI318-19 [22] and the Chinese specification GB50010-2010 [19].

The moment transfer coefficient can be derived by substituting the measured shear stress shown in Section 4.1 into the equivalent concentration reaction force equation of ACI-318, as shown in Equation (2):

$$\gamma_v = \frac{(v_u b_0 d - V) J_c}{M x b_0 d} \tag{2}$$

where v_u is the shear stress on the perimeter of the critical section of the eccentric force side, b_0 is the critical section's perimeter, d is the effective slab thickness, V is the vertical load, J_c is the property of the assumed critical section analogous to the polar moment of inertia, M is the bending moment generated by the lateral force, and x is the centroid of the shear perimeter.

Thus, the moment transfer coefficients obtained by substituting the shear stresses measured under different values of M/V into Equation (2) are listed in Table 3, and the trend is shown in Figure 23. For more comparisons, nine new groups of Ferreira et al.'s models were simulated at different M/V values. These are models with a stud diameter of 8 mm and 15 mm, and with 2, 4, and 6 studs, respectively. The details are shown in Table 3. The γ_v in ACI318-19 and Chinese specification GB50010-2010 is a parameter related only to geometry (Equation (1)). Thus, for these experimental settings, γ_v is a constant value of 0.4. The moment transfer coefficients for all of the groups of plates with different numbers and diameters of shear studs and different loading methods do not differ significantly, and can be approximated by one fitted curve to express the trend. It can be seen from Figure 23 that the FEM transfer coefficients are much smaller than the code value (0.4). Therefore, the code calculates this coefficient using only the geometry, which is safe in terms of the performance of the shear reinforcement group, but too conservative for the simulation results.

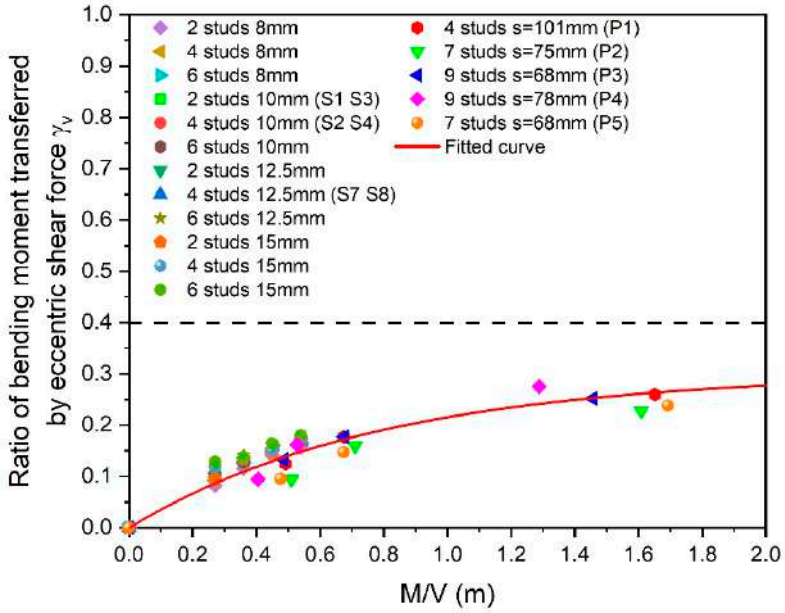

Figure 23. Fitted curve of M/V versus moment transfer coefficient.

The fitted equation for the curve of M/V versus γ_v for a slab–column connection with shear reinforcement is as follows:

$$\gamma_{vs} = 0.3 - 0.3 \times 0.285^{(\mathrm{M/V})} \quad (3)$$

As can be seen, the moment transfer coefficient is related not only to geometry, but also to other variables, such as concrete strength, reinforcement ratio, etc. These effects should be combined to determine the moment transfer coefficient's value. Therefore, the fitted equation (Equation (3)) cannot be used as a formula for calculating the moment transfer coefficient, because this paper only studies the effect of shear reinforcement and no other variables. To supplement the calculation of this coefficient, more numerical simulations of experiments with different variables are required, and it is possible to use the method of this paper to simulate experiments to refine the formula.

5. Conclusions

This study simulated experiments in which slabs equipped with shear reinforcement were subjected to concentric force and bending moment. The accuracy of the simulations was determined by comparing the crack patterns and load–displacement curves. By controlling the magnitude of the forces on the four sides of the slabs of Ferreira et al. using numerical simulations, the slabs were subjected to different bending moments. For J. Tian and K.B. Xu's slabs, the different M/V values were controlled by the amount of lateral force applied to the ends of the columns. The relationships between M/V and stresses in the critical section of the slab were obtained. The stresses in the critical section of the eccentric force side of the slab at different M/V values were substituted into the moment transfer coefficient equation of ACI318-19. Based on the results of the numerical simulation experiments, the following conclusions can be drawn:

The results of the numerical simulation are not exactly the same as the experimental values, because it was performed under ideal conditions. This is reflected in the slippage between the steel and the concrete. However, the simulation results are very similar to the experimental results. As a commercial finite element numerical simulation software platform, ABAQUS provides a good complement to the experimental limitations.

The increase of the number of shear studs on the slab can enhance the bearing capacity of the plate by 120%, but the diameter of the shear studs has little effect. When the number of shear studs configured in the slab is too many—in the two experiments in this

paper it was more than four—its contribution to the resistance to the bending moment is not significant.

The resulting γ_v is positively correlated with M/V, and the resulting trends generated by the different groups can be fitted with a line. Hence, different loading methods and different shear studs have no effect on the γ_v value. Thus, a new formula is proposed. Compared with the simulation results, the standard value of ACI318-19 related only to geometric dimensions is relatively conservative—about one time or more than the simulation results.

However, this simulation involved only two experiments. To obtain more comprehensive results, experimental models of shear reinforcement with different settings are needed. Moreover, this numerical simulation method can also study the effects of other variables—such as concrete strength, the reinforcement ratio in the slab, etc.—on the moment transfer coefficient. The formula fitted by combining the trends of the simulated γ_v values from all of these variables can only be used as the proposed formula for calculating the moment transfer coefficient.

Author Contributions: Writing—original draft, methodology, validation, formal analysis, investigation, Y.J.; review, supervision, validation, J.C.L.C. All authors have read and agreed to the published version of the manuscript.

Funding: This research was co-funded by Jeffrey C.L.Chiang, grant number SEGiIRF/2018-13/FoEBE-20/83.

Institutional Review Board Statement: Not applicable.

Informed Consent Statement: Not applicable.

Data Availability Statement: Not applicable.

Acknowledgments: The authors would like to convey their appreciation to SEGi University for sponsoring the publication of this technical paper in this journal. The authors also acknowledge the past works conducted by previous researchers on similar research areas, which have been very useful in providing ideas and inspiration for this research topic to be covered as part of the main author's study towards her doctorate degree.

Conflicts of Interest: The authors declare no conflict of interest.

Appendix A

The Chinese Code for Concrete Structure Design GB50010-2010 [19] specifies the constitutive model for concrete as follows:

The uniaxial concrete tension stress–strain curve in can be calculated according to the following formula:

$$\sigma_t = (1 - D_t)E_0\varepsilon \tag{A1}$$

$$D_t = \begin{cases} 1 - \rho_t\left[1.2 - 0.2x^5\right] & x \le 1 \\ 1 - \frac{\rho_t}{\alpha_t(x-1)^{1.7}+x} & x > 1 \end{cases} \tag{A2}$$

$$x = \frac{\varepsilon}{\varepsilon_{t,r}} \tag{A3}$$

$$\rho_t = \frac{f_{t,r}}{E_c\varepsilon_{t,r}} \tag{A4}$$

$$\alpha_t = 0.312f_{t,r}^2 \tag{A5}$$

$$\varepsilon_{t,r} = f_{t,r}^{0.54} \times 65 \times 10^{-6} \tag{A6}$$

where, α_t represents the parameter values for the descending section of the curve, $f_{t,r}$ is the representative value of uniaxial tensile strength of concrete that can be taken according to the actual structure, and the standard value of axial tensile strength is taken from Table A1. $\varepsilon_{t,r}$ is the peak tensile strain corresponding to the representative value of uniaxial

tensile strength of concrete, D_t represents the concrete uniaxial tensile damage evolution parameters, E_0 is the concrete elastic modulus, and the values are listed in Table A2.

Table A1. Standard values of axial tensile strength of concrete in GB50010.

Strength *	Concrete Strength Grade													
	C15	**C20**	**C25**	**C30**	**C35**	**C40**	**C45**	**C50**	**C55**	**C60**	**C65**	**C70**	**C75**	**C80**
f_{tk}, MPa	1.27	1.54	1.78	2.01	2.20	2.39	2.51	2.64	2.74	2.85	2.93	2.99	3.05	3.11

* The number after C indicates the concrete's cube compressive strength (MPa).

Table A2. Elastic modulus of concrete in GB50010.

f_{cu} [1]	**C15**	**C20**	**C25**	**C30**	**C35**	**C40**	**C45**	**C50**	**C55**	**C60**	**C65**	**C70**	**C75**	**C80**
E_0 [2]	2.20	2.55	2.80	3.00	3.15	3.25	3.35	3.45	3.55	3.60	3.65	3.70	3.75	3.80

[1] f_{cu} is the concrete's cube compressive strength; the number after C indicates the strength (MPa). [2] E_0 in units of ($\times 10^4$ MPa).

The uniaxial concrete compression stress–strain curve can be calculated according to the following formula:

$$\sigma_c = (1 - D_c)E_0\varepsilon \tag{A7}$$

$$D_c = \begin{cases} 1 - \frac{\rho_c n}{n - 1 + x^n} & x \le 1 \\ 1 - \frac{\rho_c}{\alpha_c(x-1)^2 + x} & x > 1 \end{cases} \tag{A8}$$

$$x = \frac{\varepsilon}{\varepsilon_{c,r}} \tag{A9}$$

$$\rho_c = \frac{f_{c,r}}{E_c\varepsilon_{c,r}} \tag{A10}$$

$$n = \frac{E_c\varepsilon_{c,r}}{E_c\varepsilon_{c,r} - f_{c,r}} \tag{A11}$$

$$\alpha_c = 0.157 f_c^{0.785} - 0.905 \tag{A12}$$

$$\varepsilon_{c,r} = 700 + 172\sqrt{f_c} \times 10^{-6} \tag{A13}$$

where α_c represents the parameter values of the falling section of the uniaxial compressive stress–strain curve for concrete; $f_{c,r}$ is the representative value of uniaxial compressive strength of the concrete, here taken as 0.76 times the cube compressive strength of the concrete; $\varepsilon_{c,r}$ is the peak strain corresponding to the uniaxial compressive strength of the concrete $f_{c,r}$; and D_c is the concrete uniaxial compressive damage evolution parameters.

In addition to the input of concrete constitutive data, the CDP model in ABAQUS requires the input of the tensile damage factor d_t and the compressive damage factor d_c, which often need to be measured experimentally. D_c and D_t in GB50010 are only damage evolution parameters, which are based on the elastic damage model, and cannot be regarded as damage factors because plastic strain results cannot be obtained. As for the choice of damage factor, there are many theories based on many researchers' trial calculations [23,24]. The formula of Sidoroff [25] was finally chosen because of its good convergence for the model.

$$d = 1 - \sqrt{\frac{\sigma}{E_0\varepsilon}} \tag{A14}$$

where σ and ε are calculated by Equations (A1) and (A7), respectively, and E_0 is the initial elastic modulus of the concrete.

Appendix B

In the table of this appendix, x is the ratio of strain to peak strain. According to the CDP model, concrete shows damage in the plastic section, so we can take x = 1 on the uniaxial compression curve of concrete and enter the plastic phase. However, for concrete, the material will drop for a short time before damage occurs, so the plastic curve partially ends at x = 3, beyond which errors occur according to numerous tests. The inelastic strain and damage factors in the first row of Tables A3–A6 are both 0, indicating that the plastic phase starts here, so it can be assumed that there is no plastic strain or damage at the beginning and that the damage factor is increasing, which is related to cracking.

Table A3. Concrete compression behavior input data of Ferreira et al.'s specimens.

x	σ (MPa)	ε_c^{in}	d (Damage Factor)
1	47.5	0	0
1.2	44.05401755	0.001048737	0.267557159
1.4	37.45498901	0.001607639	0.374737446
1.6	31.08645197	0.002160191	0.467159548
1.8	25.89451431	0.002680325	0.541500112
2	21.85589911	0.003168683	0.600385772
2.2	18.73035207	0.003631883	0.647277445
2.4	16.2870195	0.004076288	0.685089756
2.6	14.3480681	0.004506795	0.716023997
2.8	12.78458397	0.004926958	0.741693172
3	11.50435808	0.005339316	0.763276066

Table A4. Concrete tensile behavior input data of Ferreira et al.'s specimens.

x	σ (MPa)	ε_t^{in}	d (Damage Factor)
1	2.9	0	0
1.2	2.53996257	0.00006863	0.2894486
1.4	2.079222415	0.000104423	0.4048055
1.6	1.717849378	0.000137481	0.4939365
1.8	1.451784456	0.000167913	0.5613812
2	1.254346961	0.000196454	0.613218
2.2	1.104316821	0.000223689	0.6539746
2.4	0.987361044	0.000250013	0.6867401
2.6	0.894017368	0.000275686	0.7136094
2.8	0.817961603	0.000300883	0.7360268
3	0.754871444	0.000325723	0.75501

Table A5. Concrete compression behavior input data of J. Tian and K.B. Xu's specimens.

x	σ (MPa)	$\varepsilon_c{}^{in}$	d (Damage Factor)
1	22.8	0	0
1.2	22.11975209	0.001088221	0.364474397
1.4	20.62529509	0.001442294	0.431841361
1.6	18.88069762	0.001804705	0.491509816
1.8	17.16826615	0.002166044	0.542848117
2	15.60260504	0.002522491	0.586555607
2.2	14.21555962	0.002872983	0.62372602
2.4	13.00295496	0.003217661	0.655452617
2.6	11.94721089	0.00355711	0.682692646
2.8	11.02745329	0.003892027	0.706240348
3	10.22367193	0.004223077	0.726739806

Table A6. Concrete tensile behavior input data of J. Tian and K.B. Xu's specimens.

x	σ (MPa)	$\varepsilon_t{}^{in}$	d (Damage Factor)
1	2	0	0
1.2	1.873677919	0.0000509539	0.2579017
1.4	1.683850766	0.0000761831	0.3486831
1.6	1.506813457	0.000100986	0.4236659
1.8	1.356433364	0.0001249	0.4844538
2	1.231527094	0.000147966	0.5339725
2.2	1.127781845	0.000170325	0.5747877
2.4	1.040938938	0.000192122	0.6088786
2.6	0.96749296	0.000213472	0.6377221
2.8	0.904709908	0.000234466	0.6624172
3	0.850489121	0.000255175	0.683788

References

1. Elstner, R.C.; Hognestad, E. Shearing strength of reinforced concrete slabs. *ACI* **1956**, *53*, 29–58.
2. Moe, J. *Shearing Strength of Reinforced Concrete Slabs and Footings under Concentrated Loads*; Bulletin D47; Portland Cement Association, Research and Development Laboratories: Skokie, IL, USA, 1961.
3. Regan, P.E. Design for punching shear. *Struct. Eng. J.* **1974**, *52*, 197–207.
4. Regan, P.E.; Braestrup, M.W. *Punching Shear in Reinforced Concrete—A State-of-the-Art Report*; Bulletin d'Information No. 168; Comité Euro-International du Béton: Lausanne, Switzerland, 1985.
5. Hanson, N.W.; Hanson, J.M. Shear and Moment Transfer Between Concrete Slabs and Columns. *J. PCA Res. Dev. Lab.* **1968**, *10*, 2–16.
6. ACI Committee 318. *Building Code Requirements for Structural Concrete (ACI 318-70) and Commentary*; American Concrete Institute: Farmington Hills, MI, USA, 1970.
7. Chen, W.F.; Han, D.J. *Plasticity for Structural Engineers*; Springer: New York, NY, USA, 1988.
8. Simo, J.C.; Ju, J.W. Strain- and stress-based continuum damage models–I. Formulation. *Int. J. Solids Struct.* **1987**, *23*, 821–840. [CrossRef]
9. Grassl, P.; Jirásek, M. Damage-plastic model for concrete failure. *Int. J. Solids Stuct.* **2006**, *43*, 7166–7196. [CrossRef]
10. Park, H.; Choi, K. Improved strength model for interior flat plate–column connections subject to unbalanced moment. *J. Struct. Eng.* **2006**, *132*, 694–704. [CrossRef]
11. ABAQUS. *Analysis User's Manual 6.12-3*; Dassault Systems Simulia Corp.: Providence, RI, USA, 2010.
12. Xiong, J.; Ding, L.; Tian, Q. Calculation method and experimental validation of concrete damage plasticity model parameters. *J. Nanchang Univ.* **2019**, *1*, 21–26. [CrossRef]

13. Peng, X.-j.; Yu, A.-l.; Fang, Y.-z. Parametric analysis of concrete damage plasticity model. *J. Suzhou Inst. Sci. Technol.* **2010**, *3*, 40–43.
14. Li, Q.; Kuang, Y.; Guo, W. Calculation of CDP model parameters and validation of the taking method. *J. Zhengzhou Univ.* **2021**, *2*, 43–48. [CrossRef]
15. Ferreira, M.D.; Oliveira, M.H.; Sales, G.; Melo, S.A. Tests on the Punching Resistance of Flat Slabs with Unbalanced Moments. *Eng. Struct.* **2019**, *196*, 109311. [CrossRef]
16. Tian, J.; Xu, K. Experimental research on concrete slab-column joints with punching shear anchor bolts. *J. North. Jiaotong Univ.* **1999**, *6*, 73–77.
17. Genikomsou, A. Nonlinear Finite Element Analysis of Punching Shear of Reinforced Concrete Slab-Column Connection. Ph.D. Thesis, University of Waterloo, Waterloo, ON, Canada, 2015. Available online: http://hdl.handle.net/10012/10112 (accessed on 1 June 2021).
18. Lubliner, J.; Oliver, J.; Oller, S.; Onate, E. Aplastic-damage Model for Concrete. *Int. J. Solids Struct.* **1989**, *25*, 299–326. [CrossRef]
19. *GB50010-2010*; Code for Design of Concrete Structures. National Standard of the People's Republic of China: Beijing, China, 2011. (In Chinese)
20. Wu, Y.J.; Li, J.; Rui, F. An Energy Release Rate-based Plastic-damage Model for Concrete. *Int. J. Solids Struct.* **2006**, *43*, 583–612. [CrossRef]
21. European Committee for Standardization. *Design of Concrete Structures–Part 1-1: GENERAL Rules and Rules for Buildings*; EUROCODE 2: Brussels, Belgium, 2004.
22. ACI Committee 318. *ACI Building Code Requirements for Structural Concrete (ACI 318-19) and Commentary (ACI 318R-19)*; American Concrete Institute: Farmington Hills, MI, USA, 2019.
23. Guo, J.; Xu, B. Study on the Value of Damage Factor and Application of Concrete Damage Plasticity Model. *Gansu J. Sci.* **2019**, 88–92. [CrossRef]
24. Yao, F.; Guan, Q.; Wang, P. Simulation Analysis of Damage Factors Based on ABAQUS Plastic Damage Model. *Struct. Eng.* **2019**, *5*, 76–81. [CrossRef]
25. Sidoroff, F. Description of Anisotropic Damage Application to Elasticity. In *Physical Non-Linearities in Structural Analysis*; Springer: Berlin/Heidelberg, Germany, 1981.